Results in Physics 6 (2016) 606–613

Contents lists available at ScienceDirect

Results in Physics

journal homepage: www.journals.elsevier.com/results-in-physics

Super-paramagnetic core-shell material with tunable magnetic behavior by regulating electron transfer efficiency and structure stability of the shell

Wenyan Zhang [a,*], Jiahua Chen [a], Wei Wang [b,c], Lingyun Hao [a], Yaru Ni [b,c], Chunhua Lu [b,d], Zhongzi Xu [b,d]

[a] College of Material Engineering, Jinling Institute of Technology, Nanjing, PR China
[b] Jiangsu Collaborative Innovation Center for Advanced Inorganic Function Composites, Nanjing Tech University, Nanjing, PR China
[c] School of Physics and Optoelectronic Engineering, Nanjing University of Information Science & Technology, Nanjing, PR China
[d] State Key Laboratory of Materials-Oriented Chemical Engineering, College of Materials Science and Engineering, Nanjing Tech University, Nanjing, PR China

ARTICLE INFO

Article history:
Received 7 May 2016
Accepted 5 September 2016
Available online 10 September 2016

Keywords:
Super-paramagnetic
Conductivity
Magnetic shielding
Structural stability

ABSTRACT

In this work, a spherical nano core-shell material was constructed by encapsulating Fe_3O_4 microsphere into conductive polymer-metal composite shell. The Fe_3O_4 microspheres were fabricated by assembling large amounts of Fe_3O_4 nano-crystals, which endowed the microspheres with super-paramagnetic property and high saturation magnetization. The polymer-metal composite shell was constructed by inserting Pt nano-particles (NPs) into the conductive polymer polypyrrole (PPy). As size and dispersion of the Pt NPs has an important influence on their surface area and surface energy, it was effective to enlarge the interface area between PPy and Pt NPs, enhance the electron transfer efficiency of PPy/Pt composite shell, and reinforced the shell's structural stability just by tuning the size and dispersion of Pt NPs. Moreover, core-shell structure of the materials made it convenient to investigate the PPy/Pt shell's shielding effect on the Fe_3O_4 core's magnetic response to external magnetic fields. It was found that the saturation magnetization of Fe_3O_4/PPy/Pt core-shell material could be reduced by 20.5% by regulating the conductivity of the PPy/Pt shell.

Introduction

Materials could display many peculiarities and physical and chemical properties that were never observed earlier when their sizes were decreased to 1–100 nm [1]. Those special properties are known as nanometer effects, including the quantum size effects, vastly increased surface area, large chemical reactivity, and high surface energy. The nanometer effects have an astonishing influence on enlarging the surface area of materials. For example, when one used nano-cubes ($1 \times 1 \times 1$ nm^3 volume) to fill a cubic centimeter space ($1 \times 1 \times 1$ cm^3 volume), total surface area of the nano-cubes could reach up to 6000 square meters, which is larger than a football field. Owning to those nanometer effects, it is convenient to regulate the properties such as melting point, fluorescence, electrical conductivity, magnetic permeability, catalytic activity and chemical reactivity for the nano-materials, as those properties are closely related to the size of the nano-materials [2–4]. With the development of nano-science and nano-technology, the materials of nanometer scale have gradually been considered to be ideal candidates in a lot of application fields [1–4]. In recent years, magnetic nano-materials have attracted much attention in nano-material research field [5–7]. Owing to their special magnetic behavior and electrochemical properties in nanometric scale (nm), the magnetic nano-materials offer great advantages, such as superparamagnetic, high coercivity, low Curie temperature, high magnetic susceptibility, biocompatibility and low toxicity [8–18]. Those advantages endowed them with large potential in the application fields including magnetic fluids, data storage, biomedicine, biotechnology, catalysts, separation, sensors, adsorption, Li-ion batteries, microwave shielding and magnetic resonance imaging (MRI) [8–18].

It is known that the magnetic materials could display low coercive force and magnetic remanence (known as super-paramagnetic property) when their size decreased to nano-scale. Super-paramagnetic nano-materials have emerged as promising candidates for large-scale application in many fields, such as separation and adsorption, magnetically separable photocatalyst, biosensors and magneto-responsive devices, as they could be magnetized and de-magnetized just by applying or removing external

* Corresponding author.
E-mail address: wiseyanyan@jit.edu.cn (W. Zhang).

http://dx.doi.org/10.1016/j.rinp.2016.09.005
2211-3797/

magnetic fields [19–22]. However, nanometer scale generates some shortcomings for those super-paramagnetic materials as well, especially poor thermodynamic stability and aggregation problem [23–25]. Those shortcomings inhibited the application potential of nano-scaled magnetic materials. In this concern, researchers are actively engaged in solving those problems by sealing the magnetic nano-materials with conductive polymers to construct core-shell or yolk-shell composites. Conductive shell could not only protect the magnetic nano-materials and improve their environmental stability, but endow them with innovative physical and chemical properties from strong electronic interaction between the super-paramagnetic core and the polymer shell [26–29]. Conductive polymers are recognized to be an ideal candidate among those conductive shells for modifying the nano-scaled magnetic materials, considering their flexibility, tunable conductivity, as well as the functional groups at their backbone, such as amino groups in main chains of polypyrrole (PPy) and mercapto groups are contained in main chains of polythiophene [26–29].

Among various conducting polymers, PPy is recognized to be one of the most suitable candidates for encapsulating and modifying the super-paramagnetic nano-materials, due to its high electrical conductivity, easy preparation, good mechanical properties and environmental stability [29–31]. Synthesis and application of PPy based super-paramagnetic nano-composites have become one of the most active research areas in the field of polymer science and engineering. Moreover, doping or incorporating the PPy polymer with metal nanoparticles could enhance their stability further. On the one hand, numerous amino groups on the PPy chains could supply enough active sites for the loading of metal nanoparticles and promote the intimate contact between the metal nanoparticles and PPy [32,33]. On the other hand, synergism between the PPy and the metal NPs could be regulated to tune the electronic and optical properties of the conductive polymer [34–36]. It could be expected that when combing the super-paramagnetic nano-materials, PPy polymer and metal NPs together, the ternary composite materials could exhibit favorable stability and fantastic properties for the application in wide fields of technological applications.

In this work, a ternary nano-architecture was delicately designed to combine the super-paramagnetic nano-materials, PPy polymer and metal NPs together. The nano-architecture is composed of three functional components: (1) Fe_3O_4 hollow sphere as a core to endow the material with super-paramagnetic property; (2) Polypyrrole (PPy) conductive shell as shielding layer to disturb the magnetic interaction between the Fe_3O_4 core and external magnetic fields; (3) Pt NPs which were dispersed into the PPy shell. Owing to synergic effect of the three components, it is convenient to regulate the structure of PPy/Pt shell to endow the ternary nano-architecture Fe_3O_4/PPy/Pt with favorable magnetic property, electronic property and structural stability.

Materials and experiment

Preparation of Fe_3O_4 micro-spheres

The mono-dispersed Fe_3O_4 micro-spheres were synthesized by a one-pot hydrothermal method. In a typical synthesis, 0.54 g $FeCl_3{\cdot}6H_2O$ ($\geqslant$99%, Sigma-Aldrich), 1.2 g sodium citrate ($\geqslant$99.0%, Sigma-Aldrich), and 0.2 g urea ($\geqslant$99%, Sigma-Aldrich) were dissolved in distilled water (40 mL). Then, 0.2 g sodium polyacrylate (PAAS, $\geqslant$99.5%, Guoyao Corporation) was added under continuous stirring until it was totally dissolved. The solution was transferred to a 50 mL Teflon-lined autoclave, which was then sealed and maintained at 200 °C for 12 h. The product was separated by magnetic separation, washed with distilled water and absolute ethanol several times, and then dried in a vacuum oven at 60 °C overnight.

Preparation of Fe_3O_4/PPy

The Fe_3O_4/PPy were synthesized by oxidative polymerization of pyrrole (Py), as shown in Scheme 1. In a typical synthesis, 0.2 g prepared Fe_3O_4 micro-spheres and 0.05 g poly-vinylpyrrolidone (PVP) (K_{30}) were re-dispersed into 40 mL distilled water via ultrasound. 0.108 g $FeCl_3$ and 50 mL Py were sequentially added to the solution under vigorous ultrasound vibration. After reacting for 2 h, the product was separated by magnetic separation, washed with distilled water and absolute ethanol several times, and then dried in a vacuum oven at 60 °C overnight.

Preparation of Fe_3O_4/PPy/Pt catalysts

Different Fe_3O_4/PPy/Pt catalysts are all prepared by a two-step routine, as shown Scheme 1. Firstly, the Fe_3O_4/PPy spheres were synthesized by oxidative polymerization of pyrrole (Py). The PPy shell wrapped the Fe_3O_4 spheres to form a core-shell structure. Secondly, Pt NPs are introduced into the PPy layer by a different routine to form the PPy/Pt shell with various Pt NPs.

Preparation of Fe_3O_4/PPy/Pt-A catalysts

The Fe_3O_4/PPy/Pt-A was synthesized by microwave method, as shown in Scheme 1. 0.2 g prepared Fe_3O_4/PPy and 0.05 g PVP (K_{30}) were re-dispersed into 20 mL distilled water via ultrasound. Under vigorous stirring, 20 mL ethylene glycol and 1.2 g sodium citrate was dissolved into the above-prepared solution. Then 1 mL aqueous K_2PtCl_6 (Pt: 2 mg/mL) was added into above solution subsequently. The solution was transferred to a 50 mL round-bottomed flask, which was then sealed and reacted under 800 W microwave for 5 min. The product was separated by magnetic separation, washed with distilled water and absolute ethanol several times, and then dried in a vacuum oven at 60 °C overnight.

Preparation of Fe_3O_4/PPy/Pt-B catalysts

The Fe_3O_4/PPy/Pt-B was synthesized by hydrothermal method, as shown in Scheme 1. 0.2 g prepared Fe_3O_4/PPy and 0.05 g PVP (K_{30}) were re-dispersed into 40 mL distilled water via ultrasound. Under vigorous stirring, 1.2 g sodium citrate was dissolved into the above-prepared solution. Then 1 mL aqueous K_2PtCl_6 (Pt: 2 mg/mL) was added into above solution subsequently. The solution was transferred to a 50 mL Teflon-lined autoclave, which was then sealed and maintained at 200 °C for 2 h. The product was separated by magnetic separation, washed with distilled water and absolute ethanol several times, and then dried in a vacuum oven at 60 °C overnight.

Preparation of Fe_3O_4/PPy/Pt-C catalysts

The Fe_3O_4/PPy/Pt-C was synthesized by $NaBH_4$ reduction, as shown in Scheme 1. 0.2 g prepared Fe_3O_4/PPy and 0.05 g PVP (K_{30}) were re-dispersed into 40 mL distilled water via ultrasound. Under vigorous stirring, 1.2 g sodium citrate was dissolved into the above-prepared solution. Then 1 mL aqueous K_2PtCl_6 (Pt: 2 mg/mL) was added into above solution subsequently. The solution was transferred to a 50 mL round-bottomed flask. Under vigorous ultrasonic vibration, 2 mL $NaBH_4$ (0.1 M) was gradually dropped into the solution to reduce the K_2PtCl_6. The product was separated by magnetic separation, washed with distilled water and absolute ethanol several times, and then dried in a vacuum oven at 60 °C overnight.

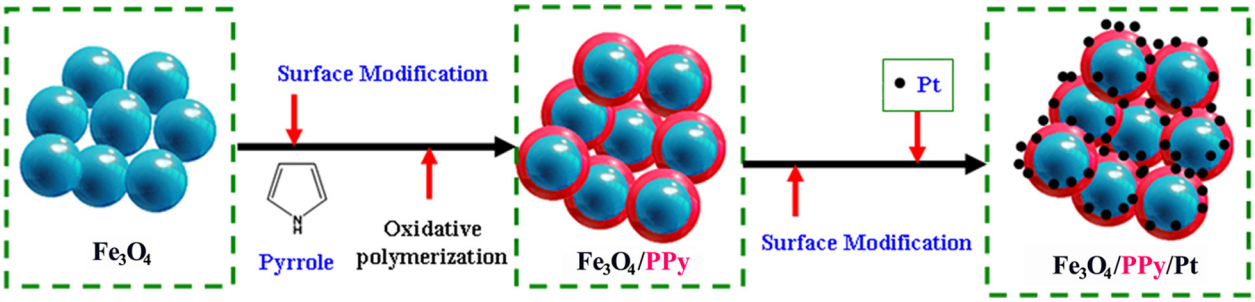

Scheme 1. Synthesis route of Fe_3O_4/PPy/Pt catalysts.

Characterization details

Transmission electron microscopy (TEM) and high-resolution TEM (HRTEM) were taken with a Tecnai-G2-F30 field emission transmission electron microscope operating at an accelerating voltage of 300 kV. The samples were dispersed in ethanol and dropped onto a carbon film supported on a copper grid for the drying process in air. X-ray diffraction (XRD) patterns of the samples were recorded on a Rigaku B/Max-RB diffractometer with a nickel filtrated Cu Kα radiation operated at 40 kV and 40 mA. Raman spectra were performed in air by high-resolution confocal μ-Raman system (Horiba JY, LabRam HR800). X-ray photoelectron spectroscopy (XPS) analysis was performed using a VG Scientific ESCALAB 210-XPS photoelectron spectrometer. Base pressure of the UHV chamber was $5 * 10^{-9}$ Torr and Mg Kα X-ray (300 W, 1253.6 eV) was used as the X-ray resource. The pass energy was 100 eV for wide range scans (survey), and 20 eV for high resolution measurements. The energy step was 1 eV for survey scans, while high resolution measurements were recorded with 0.1 eV energy step. The binding energies were referenced to the C 1s level at 284.6 eV for adventitious carbon [37]. The samples were pressed into thin sheets on Al aluminum foils. Before loading the foils into XPS analyzing chamber, they were evacuated ($5 * 10^{-5}$ Torr) for 24 h to remove the moisture and adsorbed impurity on their surface. The binding energy was selected by choosing the maximum intensity value at each peak.

The *I–V* curves of the specimens were measured by the 2-probe method on a Keithley 4200 semiconductor characterization system (electrode contact area of 2.56×10^{-6} m^2) at room temperature in air environment. Their magnetic properties were investigated by VSM magnetization curves at room temperature on a MPMS XL magnetometer made by Quantum Design Corp. Conductivity tests were carried out on The linear sweep voltammetry (LSV) measurements were measured with a scan rate of 1 mV s^{-1} on an electrochemical analyzer (CHI660A) in a homemade standard three-electrode cell. The working electrodes were prepared by drop-coating sample suspensions directly onto the pre-cleaned indium tin oxide glass (ITO glass) surface. Platinum foil was used as the counter electrode and a saturated calomel electrode (SCE) as the reference electrode. The supporting electrolyte was 0.1 M Na_2SO4 aqueous solution. The surface area of the working electrode exposed to the electrolyte was about 1 cm^2.

Results and discussion

As shown in Fig. 1(a1) and (a2), the hollow microspheres were assembled by large amounts of Fe_3O_4 NPs which were smaller than 30 nm. Fig. 1(a3) illustrates the process of how the Fe_3O_4 nanocrystals assembled to build the Fe_3O_4 microsphere during the hydrothermal process. The Fe_3O_4 NPs could provide the microspheres with super-paramagnetic property and high *Ms* value, as their sizes are approximate to single magnetic domain. Fig. 1(b2), (c2), and (d2) shows the Pt NPs inserted inside the polypyrrole (PPy) matrix to form a PPy/Pt composite layer. Pt NPs mainly expose their high-energy (1 1 1) crystal plane inside the PPy layer. The Fe_3O_4 microspheres are encapsulated by the PPy/Pt layer to build a Fe_3O_4/PPy/Pt core-shell structure. Surfaces of the Fe_3O_4/PPy/Pt are mainly composed of C, N, O and Pt elements (Fig. 2(a), survey XPS spectra). The peaks between 930 and 1030 eV are assigned to the auger electrons of carbon atoms (C KLL). As the Fe_3O_4 microspheres were enwrapped by PPy shell, peaks of Fe element is not obvious in the XPS survey spectra while the peaks of N element comes from the N atom on pyrrole ring. In addition, Fig. 1 also indicates that the Fe_3O_4 microspheres have favorable chemical stability as their sizes and morphologies maintained well when they were enwrapped by PPy and PPy/Pt shell.

The Pt NPs' size and their distribution inside the PPy are different in the Fe_3O_4/PPy/Pt-A, Fe_3O_4/PPy/Pt-B and Fe_3O_4/PPy/Pt-C samples, as shown in Fig. 1(b2, c2, d2, b3, c3, and d3). For each sample, we randomly selected three regions and recorded the HRTEM images for those regions, as shown in Fig. 1(b2–b4, c2–c4, and d2–d4). In Fe_3O_4/PPy/Pt-A, most of the Pt NPs are less than 3 nm and they distributed uniformly in the PPy layer to form a homogeneous metal-polymer network (Fig. 1(b2–b4)). In Fe_3O_4/PPy/Pt-B, the Pt NPs exhibited a wider particle-size distribution and their size increased up to 4.0 nm (Fig. 1(c2–c4)). In Fe_3O_4/PPy/Pt-C, some Pt NPs aggregated severely and the particle size grew up to 8.9 nm, as shown in Fig. 1(d2–d4). Average size of Pt NPs was calculated according to those HRTEM images in Fig. 1(b2–b4, c2–c4, and d2–d4), about 2.1 nm, 3.3 nm and 6.1 nm respectively for Fe_3O_4/PPy/Pt-A, Fe_3O_4/PPy/Pt-B and Fe_3O_4/PPy/Pt-C. In a word, in the PPy/Pt layer, size of the Pt NPs could be ranked as Fe_3O_4/PPy/Pt-A < Fe_3O_4/PPy/Pt-B < Fe_3O_4/PPy/Pt-C, while distribution uniformity of the Pt particles could be sequenced as Fe_3O_4/PPy/Pt-A > Fe_3O_4/PPy/Pt-B > Fe_3O_4/PPy/Pt-C.

HRTEM results of the samples are well supported by their XRD patterns. As shown in Fig. 2(b), eight diffraction peaks of the samples could be assigned to different crystal planes of cubic Fe_3O_4 (JCPDS#65-3107). Pt NPs diffraction peaks could also be found from the XRD patterns. Fe_3O_4/PPy/Pt-A didn't show obvious Pt diffraction peaks because the small size of Pt NPs not only decreased their diffraction intensity but broadened their diffraction width. The Fe_3O_4/PPy/Pt-B and Fe_3O_4/PPy/Pt-C apparently show the diffraction peaks of Pt (1 1 1) and Pt (2 0 0) planes of cubic Pt (JCPDS#87-0647). The diffraction intensity of Pt (1 1 1) plane is much stronger than that of the Pt (2 0 0) plane, which corroborates the HRTEM results that the Pt NPs prefer to grow along (1 1 1) crystal planes. High energy of Pt (1 1 1) facets could reinforce the interface interaction between the metal NPs and the PPy layer, thus not only strengthen the stability of the PPy layer but facilitate the electron transfer through the organic network via effective energy level matching [38,39]. Compared with Fe_3O_4/PPy/Pt-B, Fe_3O_4/PPy/Pt-C exhibits higher Pt diffraction intensity at both (1 1 1) and (2 0 0)

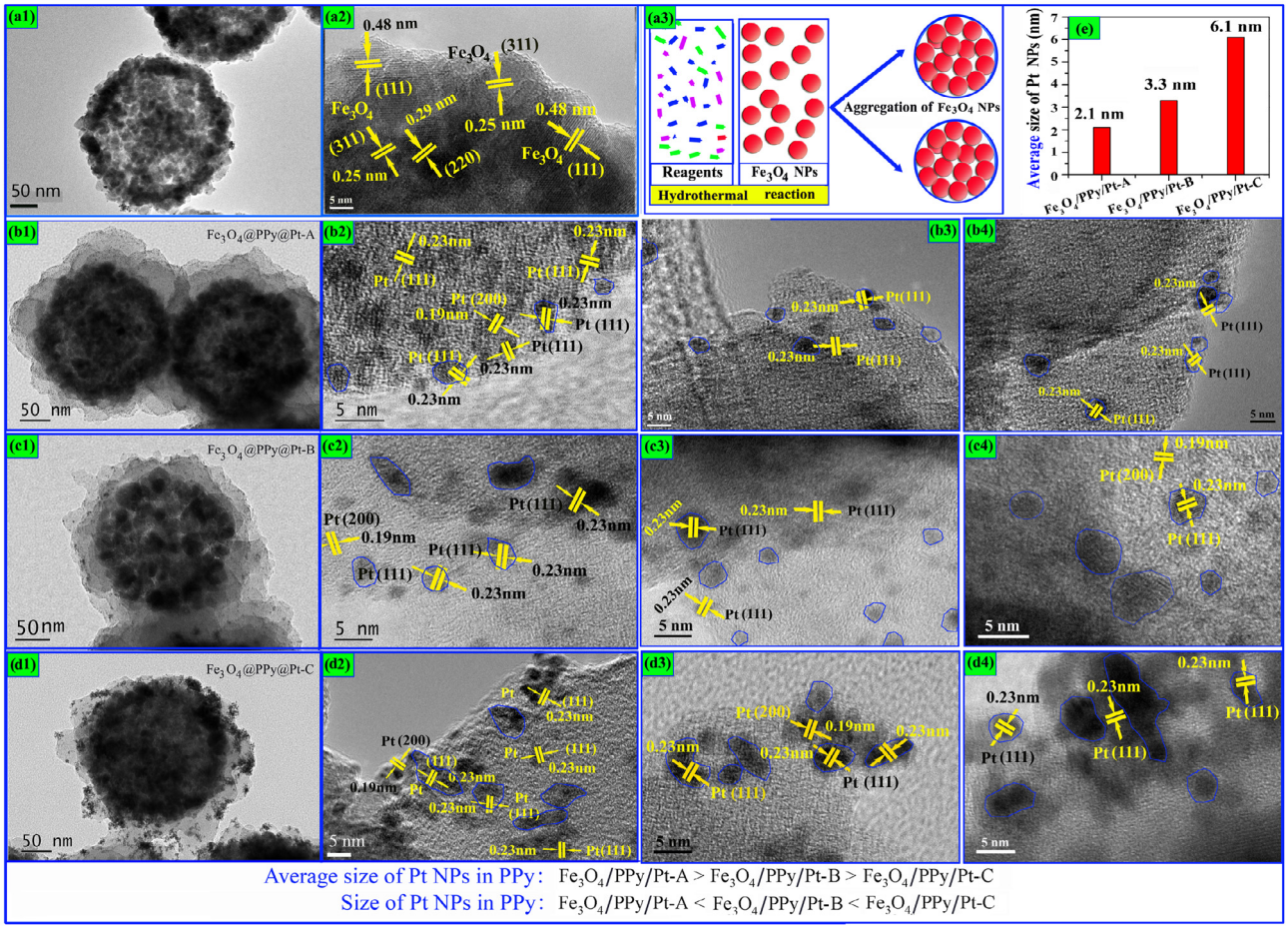

Fig. 1. TEM image and HRTEM image of (a1 and a2) Fe_3O_4 microspheres, (b1–b4) Fe_3O_4/PPy/Pt-A, (c1–c4) Fe_3O_4/PPy/Pt-B, (d1–d4) Fe_3O_4/Pt-C; (a3) Process of the Fe_3O_4 NPs assembling to form a hollow microsphere; (e) Average size of Pt NPs in Fe_3O_4/PPy/Pt-A, Fe_3O_4/PPy/Pt-B, Fe_3O_4/Pt-C.

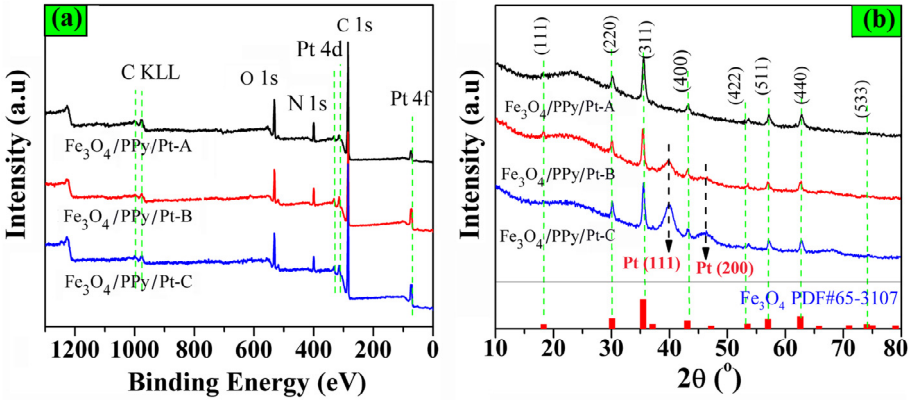

Fig. 2. (a) XPS survey spectra of Fe_3O_4/PPy/Pt-A, Fe_3O_4/PPy/Pt-B, and Fe_3O_4/Pt-C; (b) XRD patterns of Fe_3O_4/PPy/Pt-A, Fe_3O_4/PPy/Pt-B, and Fe_3O_4/Pt-C.

planes, which approves that the Pt NPs have larger size in Fe_3O_4/PPy/Pt-C.

Structures of the PPy layer were investigated by Raman spectra, which indicate conductive groups were formed in the PPy layer. As shown in Fig. 3(a) and Table 1, the strong band at 1560 cm^{-1} in the Raman spectra is assigned to the C=C conjugated bonds, which could provide the PPy layer with abundant delocalized electrons to improve its conductivity [40,41]. The bands at 983 and 930 cm^{-1} are respectively assigned to the polaron groups (—$NH^{\bullet+}$—) and bipolaron groups (=NH^{+}—), which verify moderate oxidation state of the PPy layers [30,40,41]. Moderate oxidization of PPy layers could facilitate the electron transfer through the layer, thus effectively improving their electrical conductivity [40,41]. The Fe—O stretching vibration at 662 cm^{-1} could not be detected by the FTIR spectra, as the Fe_3O_4 core was shielded by the PPy/Pt shell which prevents the infrared light penetrating into the core-shell structure.

The N 1s spectra were investigated to reveal more information of the PPy shell. In consistence with the Raman spectra, the N 1s spectra also exhibit the existence of neutral N (—NH—), polaron

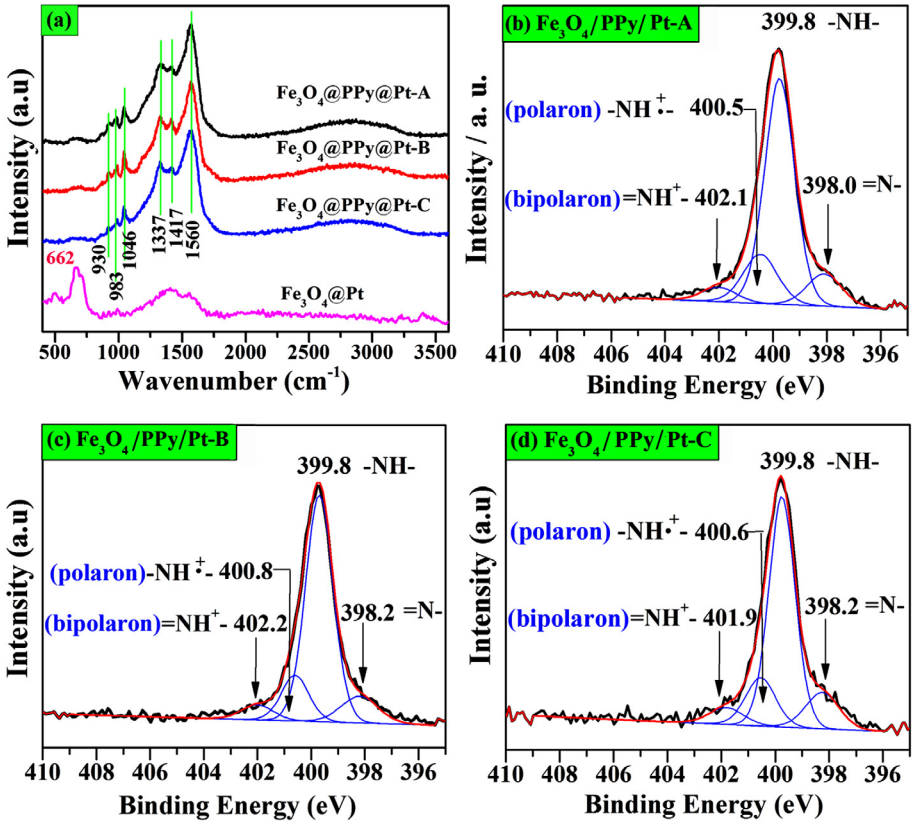

Fig. 3. (a) The Raman spectra of Fe_3O_4/PPy/Pt-A, Fe_3O_4/PPy/Pt-B, Fe_3O_4/PPy/Pt-C, Fe_3O_4/Pt; and the N 1s XPS spectra of (b) Fe_3O_4/PPy/Pt-A, (c) Fe_3O_4/PPy/Pt-B, and (d) Fe_3O_4/Pt-C.

Table 1
Assignments of the Raman bands in Fig. 3 (a).

Wavenumber (cm^{-1})	Assignment
1560	Stretching vibrations of C=C
1417	COO^- symmetric
1337	C—H stretching vibration
1046	C—H in plane bending vibration
983	Ring deformation associated with bipolaron
930	Ring deformation associated with polaron
662	Fe—O stretching vibration

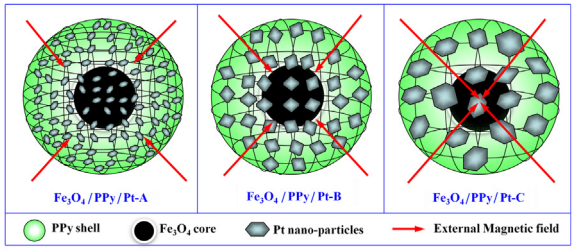

Scheme 2. Size and distribution variation of Pt NPs in the PPy/Pt shell of different specimens and their shielding effect on the external magnetic field.

(—NH•$^+$—), bipolaron (=NH$^+$—) and imine-like nitrogen (=N—) groups [40,41]. As shown in Fig. 3(b–d), the strongest peaks at 399.8 and 399.9 eV are attributed to the —NH— groups in pyrrole ring. The peaks near 400.5 eV are assigned to the polaron groups, while the peaks near 402.1 eV are assigned to the bipolaron groups. Formulas (1)–(3) illustrate the formation process of the =N—, —NH•$^+$— and =NH$^+$— groups. The PPy shell was de-protonated to a moderate oxidation state, which could be verified by the existence of a small amount of =N—, —NH•$^+$— and =NH$^+$— groups. Moderate oxidation is beneficial to improve the conductive property of PPy shell.

$$—NH— - \bullet \rightarrow —NH\bullet^+$$

$$—NH\bullet^+ - \bullet \rightarrow =NH^+—$$

$$NH\bullet^+ - H\bullet \rightarrow =N—$$

According to HRTEM, XRD and Raman results, conductive PPy/Pt shell was successfully constructed to encapsulate the Fe_3O_4 microsphere cores, as illustrated in Scheme 2. Owing to energy matching of Pt NPs and PPy layer, electrons could not only migrate in the PPy layer, but flow freely at the PPy/Pt interface from Pt NPs to PPy or vice versa, as the work function of Pt (5.5–6.4 eV) is greater than PPy (5.1 eV) [42,43]. More importantly, it is known that the materials will exhibit surface effect, small size effect and quantum confinement effect when their sizes were decreased down to nano scale. As a result, it is reasonable to expect that regulating the size and distribution uniformity of Pt NPs could modify the electronic property and structural stability of PPy/Pt shell. In order to prove that hypothesis, XPS spectra, *I–V* curves and LSV measurements investigated in detail to get more insights into their relationship (Scheme 2).

Pt 4f XPS spectra gave more details for the binding situation at the Pt/PPy interfacial junction, as shown in Fig. 4(a–f). Those Pt 4f spectra could be de-convoluted into two pairs of doublet peaks labeled with 1, 1′, 2, and 2′ (de-convoluted by symmetric component line shapes) [43,44]. The 2 and 2′ doublet peaks were attributed to metallic Pt (Pt^0), while the 1 and 1′ doublet peaks were assigned to the Pt^{2+} chemical states [43]. The Pt^0 area ratio is about

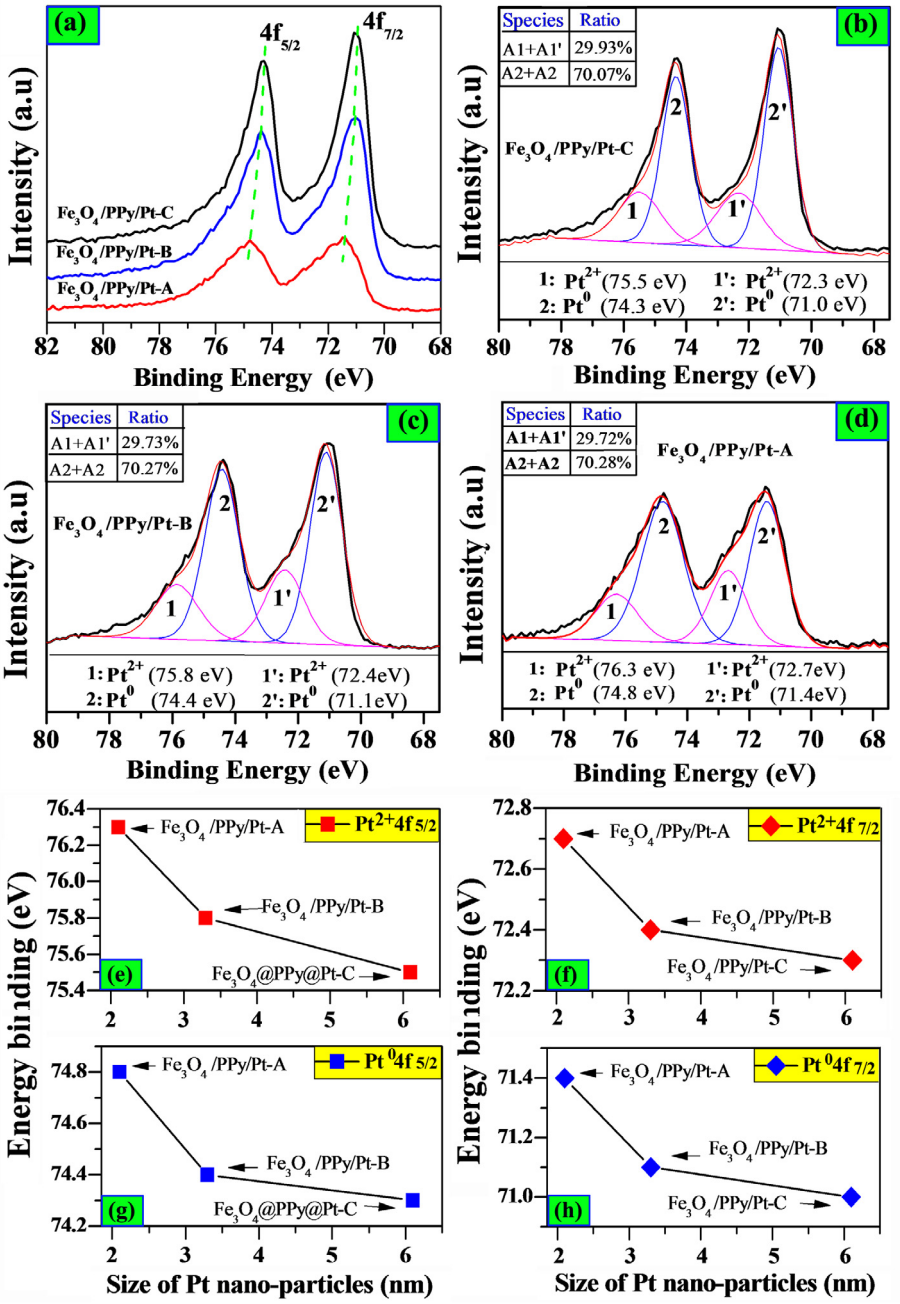

Fig. 4. (a–d) Pt 4f XPS spectra of Fe_3O_4/PPy/Pt-A, Fe_3O_4/PPy/Pt-B and Fe_3O_4/PPy/Pt-C; (e–f) Dependence of Pt $4f_{5/2}$ and Pt $4f_{7/2}$ binding energy on average size of Pt NPs.

two times higher than Pt^{2+} area ratio, as shown in the Inset Tables of Fig. 4(b–d). Thus, most Pt species existed as metallic state in the three samples. The Pt oxide species (Pt^{2+}) may be related to two reasons. On one hand, it is due to incomplete reduction of K_2PtCl_6 ($Pt^{4+} + 2e^- \rightarrow Pt^{2+}$). On the other hand, the Pt oxide species indicates electron deviation from the Pt NPs to the organic PPy layer, as the PPy layer was moderately oxidized (shown in Fig. 3) and the energy matching of Pt NPs and PPy layer [43]. Furthermore, 4f binding energies of Pt^0 and Pt^{2+} species both rose up when decreasing the Pt NPs' size and improving their distribution uniformity in the PPy layer, as shown in Fig. 4(e–f) that indicates smaller and better dispersed Pt NPs have stronger interaction with their neighboring PPy polymers. Similar phenomenon were found when depositing the Pt NPs onto the chemically modified surfaces of some carbon containing materials, such as multiwalled carbon nanotubes, gyrolytic graphite [44,45]. Such enhanced PPy/Pt interfacial coupling is closely related to the surface effect and small size effect of Pt NPs. Compared with larger and agglomerated Pt particles, the Pt NPs with smaller size and better dispersion could expose more crystal planes to neighboring PPy polymer, which could be attributed to the surface effect of nano-scale material. As a result, more interfaces were formed between the Pt NPs and the PPy layer. Besides, due to the small size effect, decreasing the size of Pt NPs could endow them with higher surface energy because their lattice periodicities were disrupted severely at the surface. The PPy/Pt layer could be reinforced to have better structure stability by larger PPy/Pt interface area and stronger interface area. *I–V* curves and LSV measurements were investigated further to study the relationship between the interface area, interface binding and the conductive property of the shell.

Fig. 5(a) shows the *I–V* curves of synthesized samples. Based on the *I–V* curves, average conductivity could be calculated to be

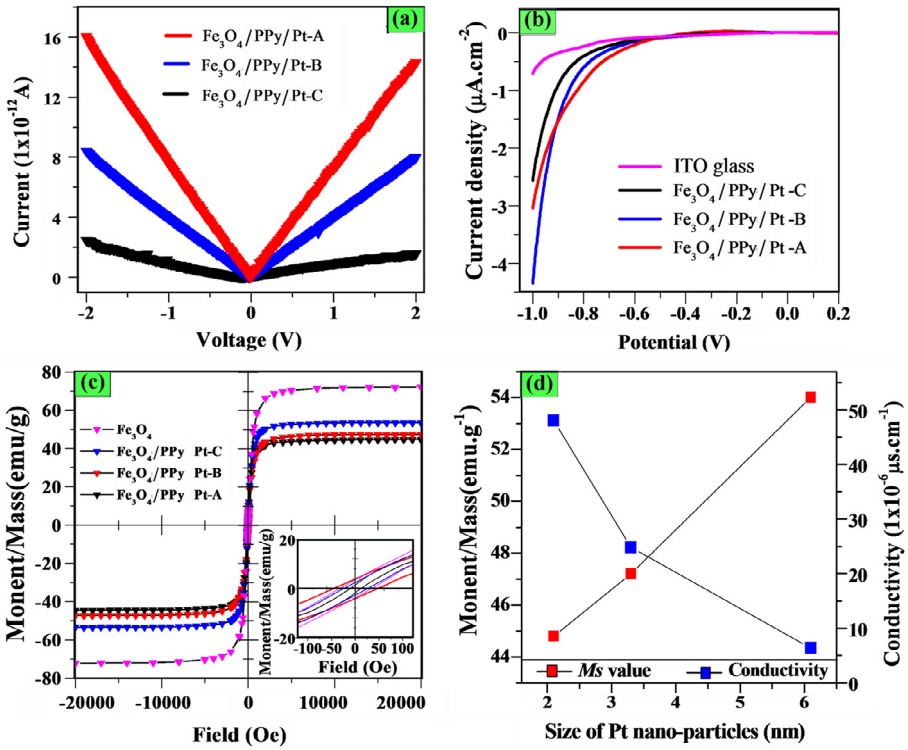

Fig. 5. (a) VSM magnetization curves, (b) dependence of saturation magnetization (*Ms*) and conductivity on the size of Pt NPs, (c) *I–V* and (d) LSV curves for the Fe_3O_4/PPy/Pt-A, Fe_3O_4/PPy/Pt-B, and Fe_3O_4/Pt-C.

48.0×10^{-6}, 24.8×10^{-6} and 6.38×10^{-6} μS cm^{-1} respectively for the Fe_3O_4/PPy/Pt-A, Fe_3O_4/PPy/Pt-B, and Fe_3O_4/Pt-C. Fig. 5(d) shows the dependence of conductivity on average Pt particle size. The results confirm the conductive properties of PPy/Pt layer were effectively improved by enlarging the area of Pt/PPy interface and strengthening the interfacial interaction to motivating the interfacial electron transfer. The LSV results also show that the electrons transferred with higher efficiency when they were in the PPy layer decorated with smaller Pt NPs (Fig. 5 (b)). When increasing applied potential, the cathodic currents grew at different rates, which could be ranked as Fe_3O_4/PPy/Pt-A > Fe_3O_4/PPy/Pt-B > Fe_3O_4/PPy/Pt-C. The LSV test also reveals that electron transportation was accelerated in the PPy/Pt shell which has a larger area and stronger interfacial binding of the Pt/PPy interface. By regulating the state of Pt NPs, it is simple and effective to tune the conductive property of the PPy/Pt layer.

The core-shell structure makes it convenient to investigate the PPy/Pt layer's shielding effect on the magnetic response of Fe_3O_4 core to external magnetic fields. As shown in Fig. 5(c), the three ternary samples all exhibit tiny remnant magnetization and coercivity. Due to their super-paramagnetic performance, the samples could be magnetized to their saturation magnetization value (***Ms***) rapidly under a low magnetic field. The saturation magnetization (***Ms***) was 44.8, 47.2 and 54 emu g^{-1} for the Fe_3O_4/PPy/Pt-A, Fe_3O_4/PPy/Pt-B, and Fe_3O_4/PPy/Pt-C, respectively (Fig. 5(c) and (d)). The results indicated that the ***Ms*** values of specimens are closely related to the size of Pt NPs and their distribution in PPy layer. The dependence of ***Ms*** value on average Pt particle size was shown in Fig. 5(d), which shows that the ***Ms*** value decreased by 20.6% when the average size of Pt NPs decreased from 6.1 to 2.1 nm. It is known that the electron-magnetic shielding effects on materials are intrinsically dependent on their conductivity, magnetic permeability and structural stability. Owing to modified conductive capability and strengthened structural stability, magnetic shielding efficiency of the PPy/Pt network could therefore be regulated to endow the PPy/Pt/Fe_3O_4 nano-architecture with different responsive sensitivities to external magnetic fields.

Conclusions

In summary, a core-shell nano-architecture Fe_3O_4/PPy/Pt was delicately designed by assembling the Fe_3O_4 microspheres, Pt NPs, and conductive PPy polymer together. The Fe_3O_4 microspheres were used as core to provide the nano-architecture with special magnetic property. The PPy/Pt shell exhibited magnetic shielding effect on the Fe_3O_4 microspheres core, and such magnetic shielding effect depended on the Pt NPs' size and their distribution inside the PPy. Modifying the distribution and reducing the size of Pt NPs could result in larger area of PPy/Pt interfaces, facilitate electron transfer inside the PPy/Pt shell, and providing the shell with reinforced structural stability. Structural variation of the PPy/Pt shell endowed themselves with different electron transfer ability and structural stability. The shell shielded the magnetic behavior of Fe_3O_4 microspheres core to different degrees because their magnetic shielding effect depends intrinsically on their electron transfer ability and structural stability. Thus, it is convenient and effective to tune the magnetic response of the Fe_3O_4/PPy/Pt nano-architecture just by regulating the structure of PPy/Pt shell. Saturation magnetization of Fe_3O_4/PPy/Pt could be reduced by 20.5% just by regulating the Pt NPs inside the PPy matrix.

Acknowledgements

This work is supported by Jiangsu Provincial Natural Science Foundation for Youths (Nos. BK20130095 and BK20150919), National Natural Science Foundation of China (No. 51502143), Prospective Joint Research Project of Jiangsu Province (No. 2014016), Foundation for Nanjing Scientific Development (No. 2012ZD002), Innovation Foundation for Scientific Research

(2014-jit-n-06), and Key University Science Research Project of Jiangsu Province (No. 15KJB430022).

References

[1] Nel A, Xia T, Mädler L, Li N. Toxic potential of materials at the nanolevel. Science 2006;311:622–7.
[2] Kyoko N, Mitsutaka F, Gene D, Mildred SD. Edge state in graphene ribbons: nanometer size effect and edge shape dependence. Phys Rev B 1996;54:17954.
[3] König M, Wiedmann S, Brüne C, Roth A, Buhmann H, Molenkamp LW, Qi XL, Zhang SC. Quantum spin hall insulator state in HgTe quantum wells. Science 2007;318:766–70.
[4] Nakano H, Ikuno T. Soft chemical synthesis of silicon nanosheets and their applications. Appl Phys Rev 2016;3:040803.
[5] Gawande MB, Brancoa PS, Varma RS. Nano-magnetite (Fe_3O_4) as a support for recyclable catalysts in the development of sustainable methodologies. Chem Soc Rev 2013;42:3371–93.
[6] Li SC, Zhang TL, Tang RZ, Qiu H, Wang CQ, Zhou ZN. Solvothermal synthesis and characterization of monodisperse superparamagnetic iron oxide nanoparticles. J Magn Magn Mater 2015;379:226–31.
[7] Angel R, Mohammed Z, Mohamed B. Magnetic (nano) materials as an useful tool for sample preparation in analytical methods. A review. Anal Methods 2013;5:4558–73.
[8] Singh K, Ohlan A, Pham VH, Balasubramaniyan R, Varshney S, Jang J, Hur SH, Choi WM, Kumar M, Dhawan SK, Kongd BS, Chung JS. Nanostructured graphene/Fe_3O_4 incorporated polyaniline as a high performance shield against electromagnetic pollution. Nanoscale 2013;5:2411–20.
[9] Mishra M, Singh AP, Singh BP, Singhc VN, Dhawan SK. Conducting ferrofluid: a high-performance microwave shielding material. J Mater Chem A 2014;2:13159–68.
[10] Pawar SP, Marathe DA, Pattabhi K, Bose S. Electromagnetic interference shielding through MWNT grafted Fe_3O_4 nanoparticles in PC/SAN blends. J Mater Chem A 2015;3:656–69.
[11] He C, Wu S, Zhao N, Shi C, Liu E, Li J. Carbon-encapsulated Fe_3O_4 nanoparticles as a high-rate lithium ion battery anode material. ACS Nano 2013;7:4459–69.
[12] Fan W, Gao W, Zhang C, Tjiu WW, Pan JS, Liu TX. Hybridization of graphene sheets and carbon-coated Fe_3O_4 nanoparticles as a synergistic adsorbent of organic dyes. J Mater Chem 2012;22:25108–15.
[13] Zhang X, Xu XW, Li TT, et al. Composite photothermal platform of polypyrrole-enveloped Fe_3O_4 nanoparticle self-assembled superstructures. ACS Appl Mater Interfaces 2014;6:14552–61.
[14] Wang H, Yuan XZ, Wu Y, et al. Facile synthesis of polypyrrole decorated reduced graphene oxide–Fe_3O_4 magnetic composites and its application for the Cr(VI) removal. Chem Eng J 2015;262:597–606.
[15] Behren S. Preparation of functional magnetic nanocomposites and hybrid materials: recent progress and future directions. Nanoscale 2011;3:877–92.
[16] Liu J, Qiao SZ, Hu QH, Lu GQ. Magnetic nanocomposites with mesoporous structures: synthesis and applications. Small 2011;7:425–43.
[17] Yuan JY, Xu YY, Müller AHE. One-dimensional magnetic inorganic–organic hybrid nanomaterials. Chem Soc Rev 2011;40:640–55.
[18] Wu W, He QG, Jiang CZ. Magnetic iron oxide nanoparticles: synthesis and surface functionalization strategies. Nanoscale Res Lett 2008;3:397–415.
[19] Li SC, Zhou ZN, Zhang TL, Jiang GT, Su R. Synthesis and characterization of Ag/Fe_3O_4 electromagnetic shielding particles. J Magn Magn Mater 2014;358–359:27–31.
[20] Li YR, Liu Q, Hong ZY, Wang HF. Magnetic separation-assistant fluorescence resonance energy transfer inhibition for highly sensitive probing of nucleolin. Anal Chem 2015;87:12183–9.
[21] Peng XQ, Zhang W, Gai LG, Jiang HH, Wang Y, Zhao LC. Dedoped Fe_3O_4/PPy nanocomposite with high anti-interfering ability for effective separation of Ag (I) from mixed metal-ion solution. Chem Eng J 2015;280:197–205.
[22] Yao TJ, Cui TY, Fang X, Yu J, Cui F, Wu J. Preparation of yolk/shell Fe_3O_4/polypyrrole composites and their applications as catalyst supports. Chem Eng J 2013;225:230–6.
[23] Long Y, Liang K, Niu JR, Yuan B, Ma JT. Pt NPs immobilized on core–shell magnetite microparticles: novel and highly efficient catalysts for the selective aerobic oxidation of ethanol and glycerol in water. Dalton Trans 2015;44:8660–8.
[24] Chen HQ, Wang W, Li GL, Li C, Zhang Y. Synthesis of P(St-MAA)-Fe_3O_4/PPy core–shell composite microspheres with conductivity and superparamagnetic behaviors. Synth Met 2011;161:1921–7.
[25] Cheng Y, Gao F, An L, Li XM, Wang GH. Different combinations of Fe_3O_4 microsphere, polypyrrole and silver as core–shell nanocomposites for adsorption and photocatalytic application. Adv Powder Technol 2014;25:1600–7.
[26] Wei JJ, Du AY, Jin F, Wang ZC, Liu XB. The preparation and high-frequency electromagnetic properties of ferrimagnetic bisphthalonitrile–Fe_3O_4 core–shell hollow microspheres. J Magn Magn Mater 2013;340:70–5.
[27] Guo J, Gu HB, Wei HG, Zhang QY, Haldolaarachchige N, Li Y, Young DP, Wei SY, Guo ZH. Magnetite-polypyrrole metacomposites: dielectric properties and magnetoresistance behavior. J Phys Chem C 2013;117:10191–202.
[28] Qi CC, Zheng JB. Novel nonenzymatic hydrogen peroxide sensor based on Fe_3O_4/PPy/Ag nanocomposites. J Electroanal Chem 2015;747:53–8.
[29] Zhao JF, Zhang SC, Liu WB, Du ZJ, Fang H. Fe_3O_4/PPy composite nanospheres as anode for lithium-ion batteries with superior cycling performance. Electrochim Acta 2014;121:428–33.
[30] Long Y, Yuan B, Niu JR, Tong X, Ma JT. Distinctive size effects of Pt nanoparticles immobilized on Fe_3O_4/PPy used as an efficient recyclable catalyst for benzylic alcohol aerobic oxidation and hydrogenation reduction of nitroaromatics. New J Chem 2015;39:1179–85.
[31] Yao TJ, Zuo Q, Wang H, Wu J, Xin BF, Cu F, Cui TY. A simple way to prepare Pd/Fe_3O_4/polypyrrole hollow capsules and their applications in catalysis. J Colloid Interface Sci 2015;450:366–73.
[32] Guo WC, Jiao J, Tian KS, Tang YF, Jia Y, Li RF, Xu ZP, Wang HY. Controllable synthesis of core–satellite Fe_3O_4/polypyrrole/Pd nanoarchitectures with aggregation-free Pd nanocrystals confined into polypyrrole satellites as magnetically recoverable and highly efficient heterogeneous catalysts. RSC Adv 2015;5:102210–8.
[33] Oliveira HPD, Andrade CAS, Melo CPD. Electrical impedance spectroscopy investigation of surfactant–magnetite–polypyrrole particles. J Colloid Interface Sci 2008;319:441–9.
[34] Chen W, Li XW, Xue G, Wang ZQ, Zou WQ. Magnetic and conducting particles: preparation of polypyrrole layer on Fe_3O_4 nanospheres. Appl Surf Sci 2003;218:215–21.
[35] Wang YQ, Zou BF, Gao T, Wu XQ, Lou SY, Zhou SM. Synthesis of orange-like Fe_3O_4/PPy composite microspheres and their excellent Cr(VI) ion removal properties. J Mater Chem 2012;22:9034–40.
[36] Gardner Todd H, Spivey James J, Kugler Edwin L, Campos Andrew, Hissam Jason C, Roy Amitava D. Structural characterization of ni-substituted hexaaluminate catalysts using EXAFS, XANES, XPS, XRD, and TPR. J Phys Chem C 2010;114:7888–94.
[37] Wojciech K, Vit R, Pavel J. Theoretical study of electronic and transport properties of PPy–Pt(111) and PPy–C(111): H interfaces. J Phys: Condens Matter 2010;22:045003.
[38] Abthagir PS, Saraswathi R. Junction properties of metal/polypyrrole Schottky barriers. J Appl Polym Sci 2001;81:2127–35.
[39] Zhong J, Gao S, Xue GB, Wang B. Study on enhancement mechanism of conductivity induced by graphene oxide for polypyrrole nanocomposites. Macromolecules 2015;48:1592–7.
[40] Park DE, Chae HS, Choi HJ, Maity A. Magnetite–polypyrrole core–shell structured microspheres and their dual stimuli-response under electric and magnetic fields. J Mater Chem C 2015;3:3150–8.
[41] Ruangchuay L, Schwank J, Sirivata A. Surface degradation of α-naphthalene sulfonate-doped polypyrrole during XPS characterization. Appl Surf Sci 2002;199:128–37.
[42] Namrata G, Bhanoth S, More PV, Jain GH, Khanna PK. Chemically designed Pt/PPy nano-composite for effective LPG gas sensor. Nanoscale 2014;6:2746–51.
[43] Su FB, Tian ZQ, Poh CK, Wang Z, Lim SH, Liu ZL, Lin JY. Pt nanoparticles supported on nitrogen-doped porous carbon nanospheres as an electrocatalyst for fuel cells. Chem Mater 2010;22:832–9.
[44] Zhang GX, Yang DQ, Sacher E. X-ray photoelectron spectroscopic analysis of Pt nanoparticles on highly oriented pyrolytic graphite. Using symmetric component line shapes. J Phys Chem C 2007;111:565–70.
[45] Yang DQ, Sacher E. Strongly enhanced interaction between evaporated Pt nanoparticles and functionalized multiwalled carbon nanotubes via plasma surface modifications: effects of physical and chemical defects. J Phys Chem C 2008;112:4075–82.